Journal of Power Sources 271 (2014) 582–588

Contents lists available at ScienceDirect

Journal of Power Sources

journal homepage: www.elsevier.com/locate/jpowsour

Facile preparation of three-dimensional multilayer porous MnO_2/reduced graphene oxide composite and its supercapacitive performance

Yiju Li, Guiling Wang, Ke Ye, Kui Cheng, Yue Pan, Peng Yan, Jinling Yin, Dianxue Cao*

Key Laboratory of Superlight Materials and Surface Technology of Ministry of Education, College of Materials Science and Chemical Engineering, Harbin Engineering University, Harbin 150001, PR china

HIGHLIGHTS

- The MnO_2/R-GO@Ni-foam composite is synthesized by a facile and scalable method.
- The MnO_2/R-GO@Ni-foam composite shows 3D multilayered porous structure.
- The MnO_2/R-GO@Ni-foam composite exhibits excellent capacitive performance.

ARTICLE INFO

Article history:
Received 25 April 2014
Received in revised form
9 August 2014
Accepted 13 August 2014
Available online 21 August 2014

Keywords:
Manganese dioxide
Reduced graphene oxide
Spray coating
Supercapacitor

ABSTRACT

Three-dimensional (3D) multilayer porous MnO_2/reduced graphene oxide composites are coated on a nickel foam substrate (denoted as MnO_2/R-GO@Ni-foam) by a facile and scalable spray method following by low temperature annealing. The composite electrodes are characterized using X-ray diffraction, scanning electron microscopy, transmission electron microscopy and Fourier transform infrared spectroscopy. The content of MnO_2 in the MnO_2/R-GO@Ni-foam composites is determined by thermal gravimetric analysis. The supercapacitive performance of the composite electroides is investigated by cyclic voltammetry, galvanostatic charge–discharge and electrochemical impedance spectroscopy. The results show that the MnO_2/R-GO@Ni-foam composite displays a high specific capacitance of 267 F g^{-1} at 0.25 A g^{-1} and excellent capacitance retention of 89.5% after 1000 cycles. This study provides a facile way for the preparation of composite electrodes for high-performance supercapacitor.

1. Introduction

During the past decades, numerous efforts have been devoted to exploit new energy storage devices with high energy and high power density that can be used in electrical vehicles. Supercapacitor emerges as a promising energy storage device, which exhibits various advantages such as high power density, long cycle life, fast charge/discharge ability and high stability [1–5]. Generally, metal oxides [6–9] and carbon materials [10–13] are the two major electrode materials of supercapacitor.

Among various metal oxides, ruthenium dioxide (RuO_2) has been widely considered as the optimum electrode material for supercapacitor [14,15]. However, its high cost and highly-toxic nature severely restrict its practical application on a large scale. Therefore, the development of low-cost metal oxides as alternative options is highly desirable. Manganese dioxide (MnO_2) has been explored as a promising electrode material for supercapacitors owing to its high theoretical capacitance, abundant source, environmental benignity and low toxicity. However, the intrinsically poor conductivity of MnO_2 (10^{-5}–10^{-6} S cm^{-1}) limited its electrochemical performance [16]. Therefore, combining MnO_2 with highly conductive carbonaceous materials to form composites has attracted significant interests as an effective way to enhance the conductivity and improve the electrochemical performance of MnO_2 [16–18].

Reduced graphene oxide (R-GO), as a kind of derivative of graphene, exhibits excellent electrical performance due to the unique ultrathin two-dimensional nanostructure. The R-GO nanosheets show a high electrical conductivity [19], high surface area and good mechanical properties. The oxygen-containing functional groups on the surface of R-GO can serve as the sites of anchoring metal ions for subsequent nucleation and growth [20,21]. Thus, integrating

* Corresponding author. Tel./fax: +86 451 82589036.
E-mail address: caodianxue@hrbeu.edu.cn (D. Cao).

http://dx.doi.org/10.1016/j.jpowsour.2014.08.048
0378-7753/

MnO_2 and R-GO to form composite materials is a desirable approach to enhance the capacitive performance of MnO_2. However, the preparation of metal oxide/graphene or reduced graphene oxide composite usually needs some special equipment (microwave oven, autoclave, etc.) [22–24] and rigorous conditions (high temperature and high pressure) [25].

Herein, we report, for the first time, a very simple and scalable method for the fabrication of 3D multilayer porous MnO_2/R-GO@Ni-foam composite electrodes at mild conditions. In the composite, R-GO nanosheets forms a 3D porous and interconnected scaffold, which serve as a conductive network and, meanwhile, provide abundant ion transport channels. This novel structure ensured the fast transportation of electrons and electrolyte ions within the whole electrode structure. The MnO_2 nanoparticles are anchored firmly on the R-GO nanosheets, prevent the agglomeration of R-GO nanosheets and provide faradic pseudocapacitance. So the MnO_2/R-GO@Ni-foam composite exhibited high specific capacitance and excellent capacitive retention.

2. Experimental

2.1. Synthesis of graphene oxide (GO)

GO was synthesized via a modified Hummers method using natural flake graphite as the raw material [26]. The typical preparation process is as follows: 1 g graphite and 0.5 g $NaNO_3$ were first mixed together in a round bottom flask and 70 ml concentrated H_2SO_4 was then added to the flask under stirring. The flask was kept in an ice bath to control the temperature below 5 °C. 3 g potassium permanganate was then gradually added to the suspension and the mixture was stirred at the temperature of 35 °C for 2 h. In the next step, 100 ml distilled water was added to dilute the solution and quickly bring the temperature to about 80 °C. After stirring at 80 °C for 0.5 h, 80 ml 5% H_2O_2 was added to the mixture to obtain GO. The GO was separated from the suspension by vacuum filtration, washed with 5% HCl and deionized water for several times, and finally dried under vacuum.

2.2. Synthesis of MnO_2/R-GO@Ni-foam composite

The MnO_2/R-GO@Ni-foam composite was prepared by simple spraying and low temperature heating method. Firstly, the nickel foam pre-treated with acetone and hydrochloric acid was dipped into a certain concentration of GO solution and heated at 200 °C for 2 h, an R-GO film was tightly coated on the surface of Ni foam. Then, a certain concentration of GO solution was sprayed uniformly onto Ni foam. After vacuum drying, the $MnCl_2$ solution and $KMnO_4$ solution were successively sprayed onto above substrate. The MnO_2 nanoparticles were formed and anchored on the surface of R-GO nanosheets through a one-step chemical reaction (eq. (1)) [27].

$$3MnCl_2 + 2KMnO_4 + 2H_2O = 5MnO_2 + 2K^+ + 6Cl^- + 4H^+ \quad (1)$$

The above coated Ni foam was immersed into deionized water to wash off the superfluous ions which adhere to the MnO_2 nanoparticles. The aforementioned procedures were repeated several times to form the 3D multilayer structure. Finally, the obtained composite was heated at 200 °C for 4 h to gain the final MnO_2/R-GO@Ni-foam composite. For comparison, the MnO_2 and R-GO coated Ni foam were also prepared using the same process and denoted as MnO_2@Ni-foam and R-GO@Ni-foam, respectively. Fig 1 shows the illustration of the preparation process of the composite electrodes. The mass loading of R-GO, MnO_2 and MnO_2/R-GO is 0.4 mg, 1.0 mg and 1.2 mg, respectively.

2.3. Characterization

The crystalline phase of the samples was measured using X-ray diffractometer (XRD, Rigaku TTR III) with Cu Kα radiation

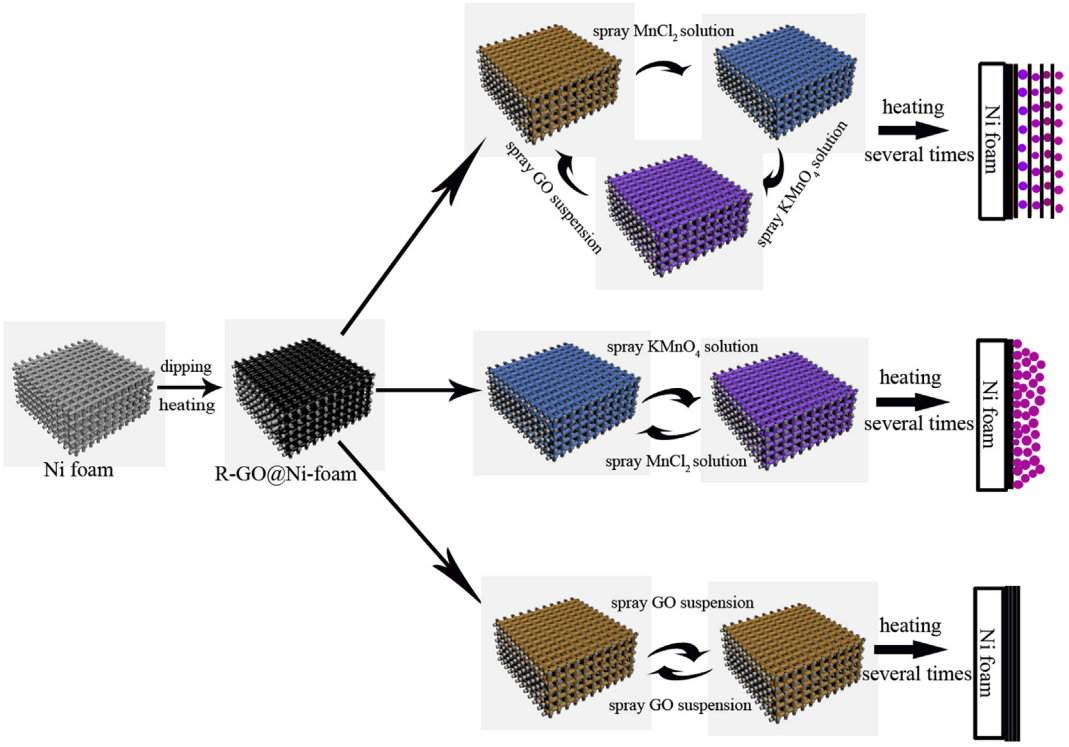

Fig. 1. The schematic illustration of the preparation of MnO_2/R-GO@Ni-foam, MnO_2@Ni-foam and R-GO@Ni-foam electrodes.

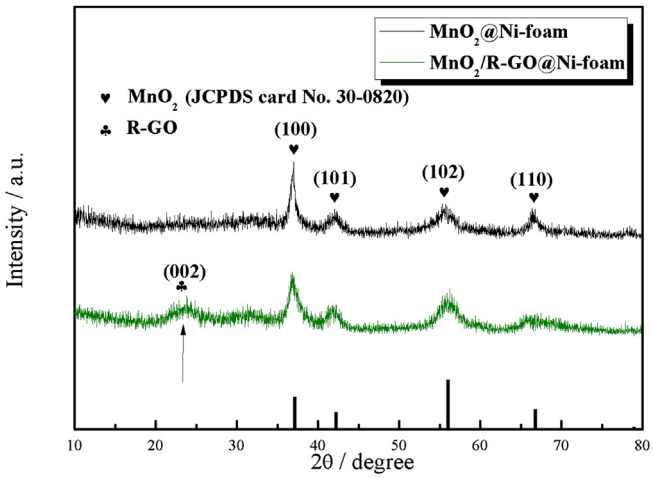

Fig. 2. The XRD patterns of MnO_2 and MnO_2/R-GO (scraped from Ni foam).

(λ = 0.1514178 nm). The morphology was examined by scanning electron microscope (SEM, JEOL JSM-6480) and transmission electron microscope (TEM, FEI Teccai G2 S-Twin, Philips). The loading of MnO_2 was measured by thermal gravimetric analysis from room temperature to 800 °C at a heating rate of 5 °C min^{-1} in air atmosphere (TGA, Netzsch STA 449C). Fourier transform infrared spectroscopy (FT-IR) analyses were carried out on a Perkin Elmer SP-100 spectrometer using a potassium bromide pellet technique.

2.4. Electrochemical measurements

All electrochemical measurements were conducted in 1 mol L^{-1} Na_2SO_4 electrolyte. The cyclic voltammetry (CV), galvanostatic charge-discharge and electrochemical impedance spectroscopy (EIS) measurements were performed in a typical three-electrode electrochemical cell by using a computerized potentiostat (VMP3/Z Bio-Logic) controlled by the EC-lab software. The prepared electrode (1 × 1 cm^2) acted as the working electrode, a platinum foil (1 × 2 cm^2) served as the counter electrode, and an Ag/AgCl electrode was used as the reference electrode. The cycle life tests were conducted on a LAND battery program-control test system. EIS measurements were performed by applying an AC voltage with 5 mV amplitude in a frequency range from 0.01 Hz to 100 kHz at the open circuit potential.

3. Results and discussion

3.1. Structure and morphology of the MnO_2/R-GO@Ni-foam composite

Fig. 2 shows the XRD patterns of MnO_2 and MnO_2/R-GO, which are scraped from the Ni foam. For the MnO_2 sample, the XRD peaks can be indexed to the diffractions of (100), (101), (102) and (110) planes of akhtenskite phase (JCPDS card No. 30-0820), suggesting the formation of akhtenskite-type MnO_2. The peaks are broad and weak which demonstrates that the crystallinity of the MnO_2 nanoparticles is relatively poor. For the sample of MnO_2/R-GO, the main XRD peaks are also indexed to the akhtenskite phase, indicating the formation of akhtenskite-type MnO_2 on the R-GO nanosheets. The broad diffraction peak at around 20–25° can be ascribed to the (002) plane of disorderedly stacked R-GO nanosheets [28]. This peak was not observed in the XRD pattern of pure MnO_2.

The morphologies of the R-GO@Ni-foam, MnO_2@Ni-foam and MnO_2/R-GO@Ni-foam composite are shown in Fig. 3. Fig. 3(A) presents the SEM image of the R-GO@Ni-foam, from which the wrinkled and thin R-GO nanosheets are revealed. The SEM image of MnO_2@Ni-foam (Fig 3(B)) shows that most of the MnO_2 nanoparticles have dimensions of 100–200 nm and aggregate together on the underlying rimous MnO_2 films. Since MnO_2 packed densely, only a very thin top layer of MnO_2 nanoparticles can participate in the charge storage process. The SEM image of MnO_2/R-GO@Ni-foam composite (Fig. 3(C)) clearly indicated a 3D multilayer

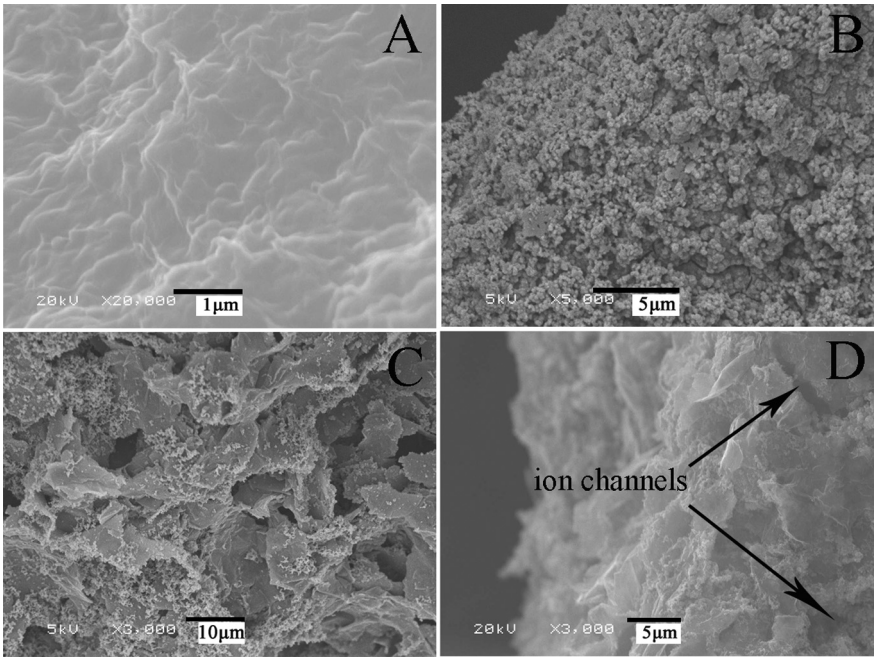

Fig. 3. The SEM images of the R-GO@Ni-foam (A), MnO_2@Ni-foam (B), MnO_2/R-GO@Ni-foam composite (C), and the cross section of MnO_2/R-GO@Ni-foam composite (D).

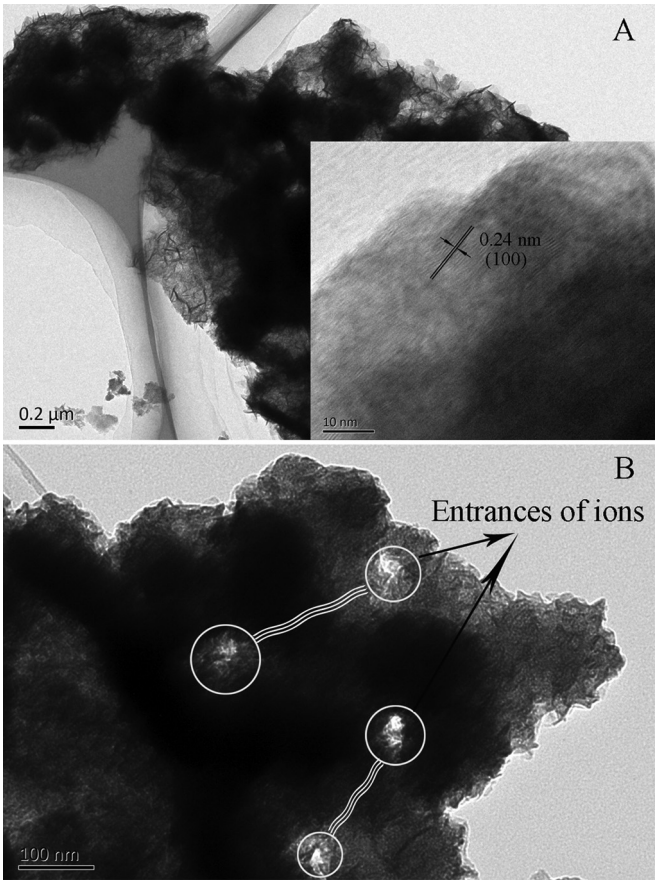

Fig. 4. The TEM images of MnO_2/R-GO@Ni-foam composite with low magnification (A) and high magnification (B). The insert in A is the HRTEM image of MnO_2.

structure, in which, MnO_2 nanoparticles anchored uniformly on the surfaces of R-GO nanosheets. The SEM image of the cross section of the 3D multilayer MnO_2/R-GO@Ni-foam composite (Fig. 3(D)) reveals the existence of narrow channels within the composite, which allow electrolyte ions easily penetrating to the inner of composite and thus accelerating the interfacial reaction.

Fig. 4 shows the TEM images of the MnO_2/R-GO@Ni-foam composite at different magnifications. It can be seen that MnO_2 nanoparticles are embedded into the porous R-GO nanosheets and there exist some micro-holes within the composites (Fig. 4(B)), which might serve as the entrance of electrolyte ions. Therefore, this unique porous structure can enables electrolyte ions effectively transporting within the electrode during the process of charge and discharge and makes the electrode have large accessible surface area, as illustrated in Fig. 5. The insert in Fig. 4(A) demonstrates a

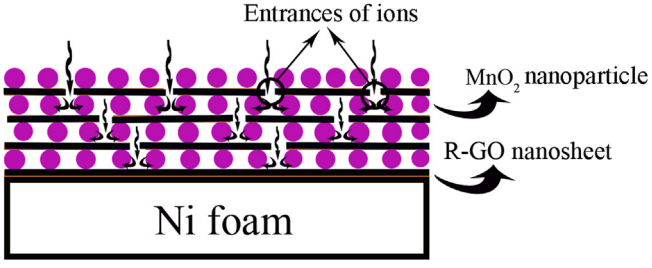

Fig. 5. The schematic diagram of the MnO_2/R-GO@Ni-foam composite structure.

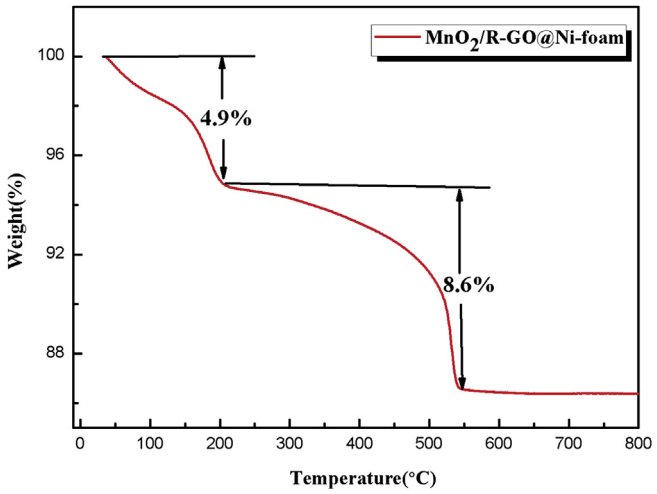

Fig. 6. The TG curve of the MnO_2/R-GO (scraped from Ni foam).

lattice spacing of about 0.24 nm, corresponding to the *d*-spacing of (100) planes of akhtenskite-type MnO_2.

Fig. 6 shows the TG curves of the MnO_2/R-GO scraped from Ni foam, The MnO_2/R-GO exhibits a 4.9% weight loss in the temperature range from 25 to 200 °C, which likely corresponds to the removal of adsorbed water. The weight loss of 8.6% in the range of 200–540 °C can be attributed to the loss of R-GO [29]. The remaining material did not show any weight loss until 800 °C, which corresponds to MnO_2. So, the percentage of MnO_2 in the MnO_2/R-GO composite is estimated to be about 91.0%.

Fig. 7 shows the FT-IR spectrum of the MnO_2/R-GO@Ni-foam composite. A broad absorption band at 3446 cm^{-1} is observed, which corresponds to the O–H stretching vibration [30]. The peaks at 2890 and 2850 cm^{-1} are identified as the stretching of $-CH_3$ and $-CH_2$, respectively. Another absorption peak located at 1624 cm^{-1} can be attributed to the vibration of the adsorbed aromatic C=C [30]. The weak vibration of C–O–C peak is appeared at 1053 cm^{-1} [31]. The absorption peak at 1365 cm^{-1} can be assigned to the typical stretching vibrations of C–OH. The peak at approximately 560 cm^{-1} corresponds to the Mn–O bond [32]. So the FT-IR spectrum further reveals that MnO_2 nanoparticles, anchoring between the R-GO nanosheets, have been successfully synthesized.

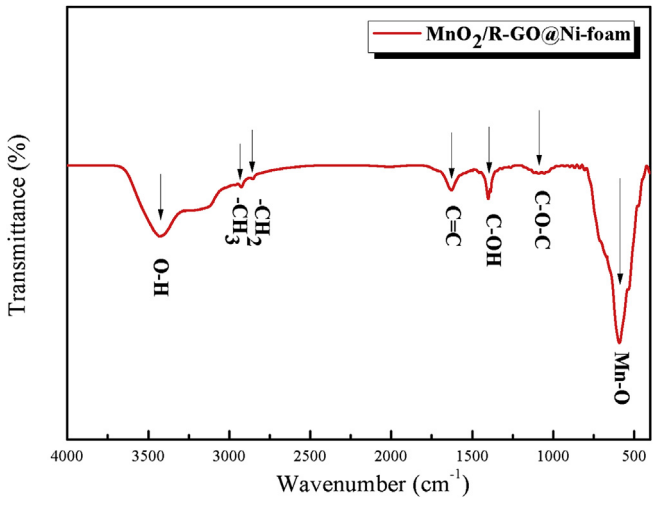

Fig. 7. The FT-IR spectrum of the MnO_2/R-GO (scraped from Ni foam).

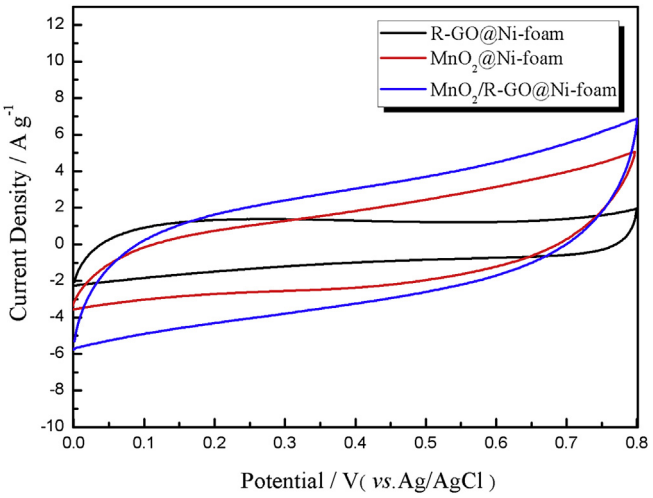

Fig. 8. CV curves of the R-GO@Ni-foam, MnO_2@Ni-foam and MnO_2/R-GO@Ni-foam composite at the same scan rate of 20 mV s^{-1}.

3.2. Electrochemical performance of MnO_2/R-GO@Ni-foam composite

The electrochemical performance of RGO@Ni-foam, MnO_2@Ni-foam and MnO_2/R-GO@Ni-foam composite were investigated by cycle voltammetry at the same scan rate of 20 mV s^{-1} within the potential range of 0–0.8 V. For comparison, the measured currents were normalized to the total mass of electroactive material for each electrode. The results are shown in Fig 8. The CV of the R-GO@Ni-foam electrode exhibits nearly a rectangle shape implying the good double layer capacitive behavior. While the CV of the MnO_2@Ni-foam and MnO_2/R-GO@Ni-foam composite show the quasi-rectangle shapes. More importantly, the CV area of the MnO_2/R-GO@Ni-foam composite is much larger than that of the R-GO@Ni-foam and MnO_2@Ni-foam electrode. Since the specific capacitance of an electrode is directly proportional to the area of its CV, the results suggest that the MnO_2/R-GO@Ni-foam composite has a larger specific capacitance than the R-GO@Ni-foam and MnO_2@Ni-foam electrode.

The galvanostatic charge–discharge tests were performed to obtain the specific capacitance of the R-GO@Ni-foam, MnO_2@Ni-foam and MnO_2/R-GO@Ni-foam composite at different current densities and the results are shown in Fig. 9(A)–(C). The specific capacitances (C) of the electrodes were calculated according to the following equation:

$$C = \frac{I_d \times \Delta t}{V} \quad (2)$$

Where I_d (A g^{-1}) is the discharge current density, Δt (s) is the discharge time and V (V) is the discharge voltage range. The obtained specific capacitances are given in Fig 9(D). As seen, the specific capacitance of the MnO_2/R-GO@Ni-foam composite is 267 F g^{-1} at a current density of 0.25 A g^{-1}, and is higher than that of MnO_2@Ni-foam (198 F g^{-1}) and R-GO@Ni-foam (90 F g^{-1}). Zhang et al. [33] synthetized reduced graphene oxide-MnO_2 nanosheet composite, which exhibits a specific capacitance of 188 F g^{-1} at 0.25 A g^{-1}. Mao et al. [34] reported that the graphene/flower-like MnO_2 composite and graphene/needle-like MnO_2 composite present 280 F g^{-1} and 260 F g^{-1} at 0.2 A g^{-1}, respectively. Zhu et al. [35] demonstrated that the specific capacitance of graphene/honeycomb-like MnO_2 composite reaches 210 F g^{-1} at 0.5 A g^{-1}. The specific capacitance of our MnO_2/R-GO@Ni-foam is comparable to that of the graphene/MnO_2 composites reported in the above-mentioned literatures. The enhanced capacitive performance of the MnO_2/R-GO@Ni-foam electrode can be attributed to the synergistic effect between R-GO nanosheets and MnO_2 nanoparticles. When the discharge current density increased from 0.25 A g^{-1} to 5 A g^{-1} (20 times), the capacitance retention of the MnO_2/R-GO@Ni-foam composite is 58.8%, which is much larger than that of MnO_2@Ni-foam (31.6%).

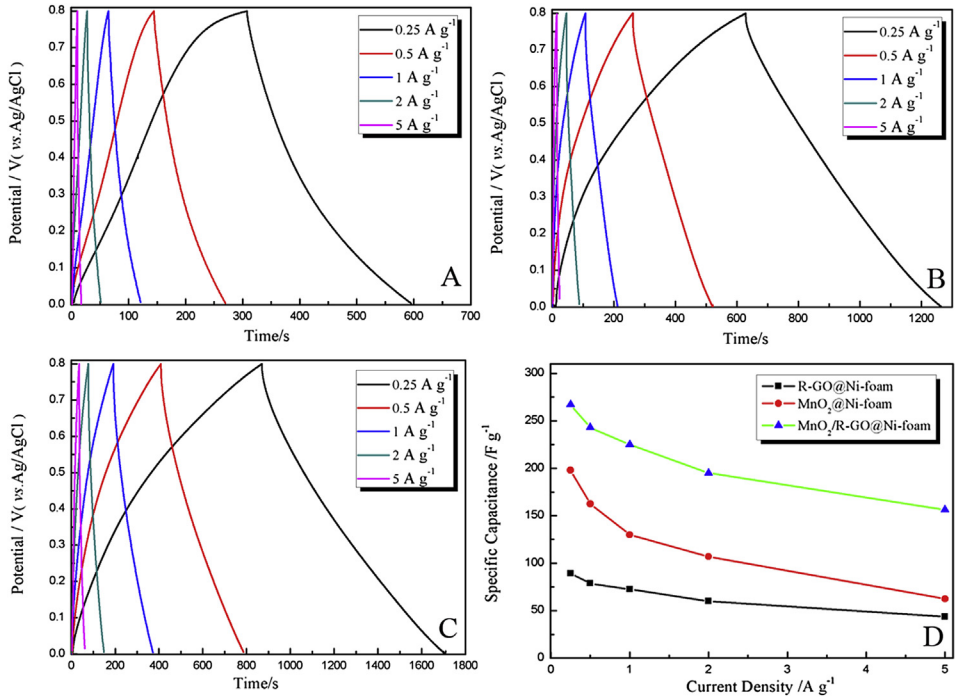

Fig. 9. The charge/discharge curves of R-GO@Ni-foam (A), MnO_2@Ni-foam (B) MnO_2/R-GO@Ni-foam composite (C) and their rate performance (D).

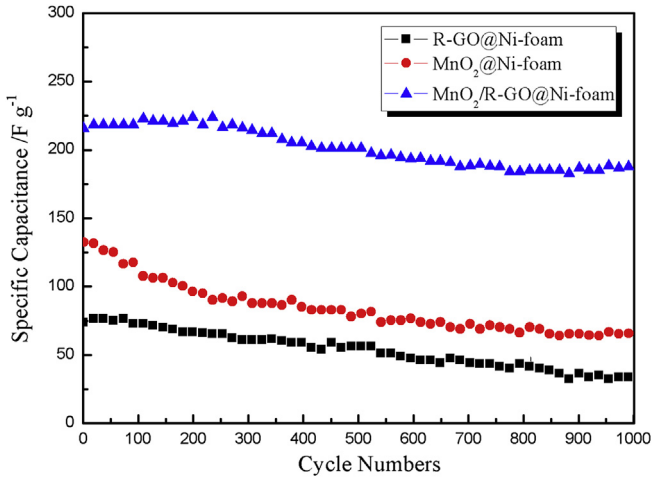

Fig. 10. The cycling performance of the R-GO@Ni-foam, MnO_2@Ni-foam and MnO_2/R-GO@Ni-foam composite.

Interestingly, the specific capacitance of MnO_2/R-GO@Ni-foam composite is higher than the total specific capacitance of the individual MnO_2@Ni-foam and R-GO@Ni-foam at high charge/discharge current densities. For example, at 2 A g^{-1}, the MnO_2/R-GO@Ni-foam composite shows a specific capacitance of 195 F g^{-1}, which is larger than the sum of the MnO_2@Ni-foam (107 F g^{-1}) and R-GO@Ni-foam (60 F g^{-1}). These results indicate that the synergistic effect between MnO_2 nanoparticles and R-GO nanosheets is favorable for high rate capability. Firstly, the anchored MnO_2 nanoparticles, serving as the spacers between adjacent R-GO nanosheets, prevent the R-GO nanosheets from agglomerating and enable electrolyte ions to access even the inner part of porous R-GO nanosheets. Secondly, the 3D multilayer R-GO nanosheets with uniformly anchored MnO_2 nanoparticles link each other and serve as the conductive scaffold, which can facilitate the electron transfer from R-GO to MnO_2 nanoparticles, resulting in rapid redox reaction of MnO_2. So, the unique structure of the MnO_2/R-GO@Ni-foam electrode ensures the utilization of both MnO_2 nanoparticles and R-GO, leading to the enhanced capacitive performance.

The cycling performances of the R-GO@Ni-foam, MnO_2@Ni-foam and MnO_2/R-GO@Ni-foam electrode were tested at the current density of 1 A g^{-1} for 1000 cycles. The results are shown in Fig 10. The R-GO@Ni-foam and MnO_2@Ni-foam electrodes show a pronounced decay in specific capacitance and the capacitance retention was 48.3% and 57.7% after 1000 cycles, respectively, which is likely due to agglomeration of the adjacent R-GO nanosheets [36] and mechanical expansion of MnO_2 during the ion insertion/removal process [17]. As for the MnO_2/R-GO@Ni-foam composite electrode, the capacitive retention reaches 89.5% after 1000 cycles, displaying a good cycling stability. This can be attributed to the intimate contact between the R-GO nanosheets and MnO_2 nanoparticles.

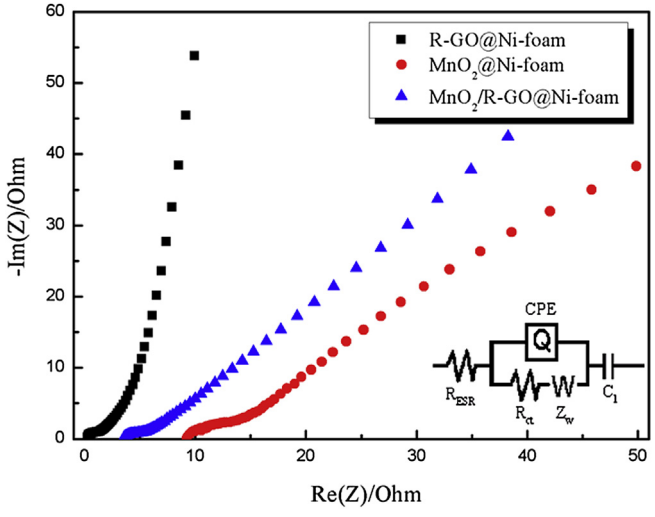

Fig. 11. EIS curves of the R-GO@Ni-foam, MnO_2@Ni-foam and MnO_2/R-GO@Ni-foam composite. The insert is the electrical equivalent circuit.

EIS was also measured for the R-GO@Ni-foam, MnO_2@Ni-foam and MnO_2/R-GO@Ni-foam electrodes and fitted using the electrical equivalent circuit given in Fig. 11. In the circuit, R_{ESR} is the sum of resistance of electrolyte, electrode material and the contact resistance at the interface of the active material/current collector. CPE represents the constant phase element, which models the double-layer capacitance (C_{dl}). R_{ct} is the charge transfer resistance, Z_w is the Warburg impedance and C_l is the limit capacitance. The R_{ESR} values of R-GO@Ni-foam, MnO_2@Ni-foam and MnO_2/R-GO@Ni-foam composite are 0.25, 8.8, and 3.1 Ω, respectively, implying that the electrical conductivity of the MnO_2/R-GO@Ni-foam composite is remarkably higher than MnO_2@Ni-foam, but lower than R-GO@Ni-foam. The R_{ct} values for the R-GO@Ni-foam, MnO_2@Ni-foam and MnO_2/R-GO@Ni-foam composite are 0.78 Ω, 7.4 Ω and 1.2 Ω, respectively, indicating that the MnO_2/R-GO@Ni-foam composite electrode has much faster kinetics than that of the MnO_2@Ni-foam, which benefits to the capacitive performance of composite materials, particularly at high charge/discharge current densities [37].

4. Conclusions

In this study, a facile and scalable spraying method has been developed to fabricate the 3D multilayer porous MnO_2/R-GO@Ni-foam composite electrode. The MnO_2/R-GO@Ni-foam composite exhibited a synergistic effect between the R-GO nanosheets and MnO_2 nanoparticles, leading to an enhanced capacitive performance. The specific capacitance of the MnO_2/R-GO@Ni-foam composite (267 F g^{-1} at 0.25 A g^{-1}) is larger than that of R-GO@Ni-foam (90 F g^{-1} at 0.25 A g^{-1}) and MnO_2@Ni-foam (198 F g^{-1} at 0.25 A g^{-1}). In addition, the MnO_2/R-GO@Ni-foam composite also exhibits improved rate capability and cycling stability (~89.5% after 1000 cycles). The enhanced capacitive performance can be attributed to the interconnected R-GO nanosheets scaffolds, which serve as conducting networks and provide ions transport channels. So both the electron transportation and ion transportation are accelerated. Besides, the MnO_2 nanoparticles embed firmly into the interspace of R-GO nanosheets preventing the agglomeration of R-GO nanosheets.

Acknowledgments

We gratefully acknowledge the financial support of this research by the Heilongjiang Postdoctoral Fund (LBH-Z13059), The National Natural Science Foundation of China (21403044) and Fundamental Research Funds for the Central Universities (HEUCF201403019).

References

[1] M. Meyyappan, J. Vac. Sci. Technol. A 31 (2013) 050803.
[2] J. Zhang, X. Zhao, ChemSusChem 5 (2012) 818–841.
[3] G. Wang, L. Zhang, J. Zhang, Chem. Soc. Rev. 41 (2012) 797–828.
[4] C. Liu, F. Li, L.P. Ma, H.M. Cheng, Adv. Mater. 22 (2010) E28–E62.
[5] M. Winter, R.J. Brodd, Chem. Rev. 104 (2004) 4245–4270.
[6] L. Chen, Y. Hou, J. Kang, C. Mingwei, J. Mater. Chem. A 2 (2014) 8448–8455.

[7] Q. Yang, Z. Lu, J. Liu, X. Lei, Z. Chang, L. Luo, X. Sun, Prog. Nat. Sci. Mater. Int. 23 (2013) 351–366.
[8] R.B. Rakhi, W. Chen, M. Hedhili, D. Cha, H.N. Alshareef, ACS Appl. Mater. Interfaces 6 (2014) 4196–4206.
[9] L. Zang, J. Zhu, Y. Xia, J. Mater. Eng. Perform. 23 (2014) 679–683.
[10] L.L. Zhang, X. Zhao, Chem. Soc. Rev. 38 (2009) 2520–2531.
[11] Y. Wang, Z. Shi, Y. Huang, Y. Ma, C. Wang, M. Chen, Y. Chen, J. Phys. Chem. C 113 (2009) 13103–13107.
[12] H. Jiang, P.S. Lee, C. Li, Energy Environ. Sci. 6 (2013) 41–53.
[13] M. Li, J. Xue, J. Phys. Chem. C 118 (2014) 2507–2517.
[14] Z. Zhou, Y. Zhu, Z. Wu, F. Lu, M. Jing, X. Ji, RSC Adv. 4 (2014) 6927–6932.
[15] Z.S. Wu, D.W. Wang, W. Ren, J. Zhao, G. Zhou, F. Li, H.M. Cheng, Adv. Funct. Mater. 20 (2010) 3595–3602.
[16] T. Zhai, F. Wang, M. Yu, S. Xie, C. Liang, C. Li, F. Xiao, R. Tang, Q. Wu, X. Lu, Nanoscale 5 (2013) 6790–6796.
[17] Y. He, W. Chen, X. Li, Z. Zhang, J. Fu, C. Zhao, E. Xie, ACS Nano 7 (2012) 174–182.
[18] G. Yu, L. Hu, M. Vosgueritchian, H. Wang, X. Xie, J.R. McDonough, X. Cui, Y. Cui, Z. Bao, Nano Lett. 11 (2011) 2905–2911.
[19] J. Chen, C. Li, G. Shi, J. Phys. Chem. Lett. 4 (2013) 1244–1253.
[20] D. Chen, H. Feng, J. Li, Chem. Rev. 112 (2012) 6027–6053.
[21] Y. Zhu, D.K. James, J.M. Tour, Adv. Mater. 24 (2012) 4924–4955.
[22] Z. Li, Y. Mi, X. Liu, S. Liu, S. Yang, J. Wang, J. Mater. Chem. 21 (2011) 14706–14711.
[23] Z. Li, J. Wang, S. Liu, X. Liu, S. Yang, J. Power Sources 196 (2011) 8160–8165.
[24] J. Yan, Z. Fan, T. Wei, W. Qian, M. Zhang, F. Wei, Carbon 48 (2010) 3825–3833.
[25] K. Dai, L. Lu, C. Liang, J. Dai, Q. Liu, Y. Zhang, G. Zhu, Z. Liu, Electrochim. Acta 116 (2014) 111–117.
[26] D.C. Marcano, D.V. Kosynkin, J.M. Berlin, A. Sinitskii, Z. Sun, A. Slesarev, L.B. Alemany, W. Lu, J.M. Tour, ACS Nano 4 (2010) 4806–4814.
[27] V. Mathew, J. Lim, J. Kang, J. Gim, A.K. Rai, J. Kim, Electrochem. Commun. 13 (2011) 730–733.
[28] F. Tu, S. Liu, T. Wu, G. Jin, C. Pan, Powder Technol. 253 (2014) 580–583.
[29] M.J. Tadjer, M.A. Mastro, J.M. Rojo, A.B. Mojena, F. Calle, F.J. Kub, C.R. Eddy Jr., J. Electron. Mater. 43 (2014) 1188–1193.
[30] Y. Zhang, H. Liu, Z. Zhu, K.-w. Wong, R. Mi, J. Mei, W.-m. Lau, Electrochim. Acta 108 (2013) 465–471.
[31] Y. Liu, Y. Ying, Y. Mao, L. Gu, Y. Wang, X. Peng, Nanoscale 5 (2013) 9134–9140.
[32] S. Deng, D. Sun, C. Wu, H. Wang, J. Liu, Y. Sun, H. Yan, Electrochim. Acta 111 (2013) 707–712.
[33] J. Zhang, J. Jiang, X. Zhao, J. Phys. Chem. C 115 (2011) 6448–6454.
[34] L. Mao, K. Zhang, H.S.O. Chan, J. Wu, J. Mater. Chem. 22 (2012) 1845–1851.
[35] J. Zhu, J. He, ACS Appl. Mater. Interfaces 4 (2012) 1770–1776.
[36] J. Yan, T. Wei, B. Shao, F. Ma, Z. Fan, M. Zhang, C. Zheng, Y. Shang, W. Qian, F. Wei, Carbon 48 (2010) 1731–1737.
[37] J. Zhang, X. Zhao, Carbon 52 (2013) 1–9.